

Nanoscale Au-In Alloy-Oxide Core-Shell Particles as Electrocatalysts for Efficient Hydroquinone Detection

C. Medina-Plaza,^{a,c} M. L. Rodriguez-Mendez,^{a*} P. Sutter,^b X. Tong,^c and E. Sutter^{d*}

^a*Department of Inorganic Chemistry, Engineers School, Universidad de Valladolid, 47011 Valladolid, Spain.*

^b*Department of Electrical and Computer Engineering, University of Nebraska-Lincoln, Lincoln, NE 68588, USA.*

^c*Center for Functional Nanomaterials, Brookhaven National Laboratory, Upton, NY 11978, USA.*

^d*Department of Mechanical and Materials Engineering, University of Nebraska-Lincoln, Lincoln, NE 68588, USA.*

Abstract

The presence of hydroquinone (HQ), a phenol, ubiquitous in nature and widely used in industry needs to be monitored due to its toxicity to the environment. Here we demonstrate efficient detection of HQ using simple, fast and non-invasive electrochemical measurements on ITO electrodes modified with nanoparticles comprising bimetallic Au-In cores and mixed Au-In oxide shells. While bare ITO electrodes show very low activity for the detection of HQ, their modification with Au-In core-shell nanoparticles induces a pronounced shift of the oxidation peak to lower potentials, *i.e.*, facilitated oxidation. The response of the different electrodes was correlated with the initial composition of the bimetallic nanoparticle cores, which in turn determined the amount of Au and In stabilized on the surface of the amorphous Au-In oxide shells available for the electrochemical reaction. While adding core-shell nanostructures with different compositions of the alloy core facilitates the electrocatalytic (reduction-) oxidation of HQ, the activity is highest for particles with AuIn cores (*i.e.*, a Au:In ratio of 1). This optimal system is found to follow a single pathway, the two-electron oxidation of the quinone-hydroquinone couple, which gives rise to high oxidation peaks, and is most effective in facilitating the electrode-to-analyte charge transfer and thus detection. The limits of detection (LOD) decreased when increasing the amount of Au exposed on the surface of the amorphous Au-In oxide shells. The LODs were in the range of 10^{-5} - 10^{-6} M and were lower than those obtained using bulk Au.

Keywords: amorphous mixed gold-indium oxide, alloy nanoparticles, electrochemical catalysis, transmission electron microscopy.

Corresponding authors: M.L. Rodriguez-Mendez, Tel.: +34983423540, Email: mluz@eii.uva.es, and E. Sutter, Tel.: (402) 472 2465, Email: esutter@unl.edu

1. Introduction

Phenolic compounds are a large family of molecules, which have attracted great interest in the food industry due to their antioxidant capacity and potential health benefits.¹ On the negative side, phenolic compounds occur as byproducts of a variety of industries and are ubiquitous in the environment. They are classified as hazardous materials and are particularly toxic to the environment. Hydroquinone (HQ) is one example of this broader class of phenolic compounds that is important in a number of biological processes, as well as in industrial products including dyes, cosmetics, pesticides, paper manufacturing, and photographic developers.² The detection and assessment of hydroquinone can be carried out using traditional techniques such as fluorescence,³ chemiluminescence,⁴ and high performance liquid chromatography,⁵ among others. Compared to these methods, which require complex instrumentation, electrochemical methods could provide compact and relatively inexpensive setups with fast response for real-time analysis in the field. Conventional (*i.e.*, metallic or glassy carbon) electrodes, however, are not suitable for the detection of phenols due to their poor electrochemical response.⁶ One possible strategy for preparing efficient sensing devices is the modification of the electrode surface with nanomaterials. Electrodes modified with metal nanoparticles are very promising as they show unique electronic and catalytic properties.⁷ Au nanoparticles among other noble metals, have demonstrated electrocatalytic enhancement in various processes: fuel cells,^{8,9} sensors,^{10,11} food analysis,^{12,13} and photovoltaic devices.^{14,15} Au nanoclusters provide even higher catalytic activity¹⁶ as well as other benefits, for instance stabilization against dissolution under potential cycling regimes of oxygen-reduction fuel-cell electrocatalysts.¹⁷ Small Au nanoparticles and nanoclusters require complicated synthesis and are hard to stabilize in their active configuration, as they sinter easily and their catalytic properties degrade as a result of the size increase. We recently developed

a simple approach for the formation of stable Au-based catalysts, in which the active sites are small gold clusters anchored in an amorphous Au-In oxide matrix. Au-In alloy nanoparticles prepared by metal evaporation (or other methods) transform into metal alloy-oxide core-shell structures during oxidation at room temperature.¹⁸ AuIn alloy nanoparticles terminated by gold-containing oxide shells were found to be active in the conversion of CO and O₂ to CO₂ near room temperature, as well as stable against sintering up to high temperatures (>300°C), and thus show promising properties for heterogeneous catalysis.

Here we use arrays of high-surface area Au_xIn_{1-x} core-shell nanostructures with different alloy composition, x, prepared by room temperature oxidation of Au-In alloys with different composition, to modify standard indium tin oxide (ITO) electrodes and investigate the oxidation of hydroquinone in aqueous solutions. Our results show that oxidized Au-In core-shell nanoparticles present electrocatalytic activity towards the detection of hydroquinone. We find that the electrocatalytic properties are directly influenced by the Au:In ratio, as demonstrated by a significant decrease in the oxidation potential at which oxidation of hydroquinone takes place.

2. Materials and Methods

Bimetallic Au-In alloy nanoparticles with different compositions were formed by sequential room temperature magnetron sputtering of controlled amounts of Au and In onto different substrates: indium tin oxide (ITO) electrodes (for electrocatalytic measurements), as well as Ge (111) and amorphous carbon and few-layer graphene membranes supported on standard TEM grids for materials characterization. Pure In and Au nanoparticles for control experiments were prepared by sputtering of only In and Au, respectively, under the same conditions. Different compositions of the Au-In alloy in the nanostructures were obtained by depositing a fixed amount of Au (2nm equivalent thickness), followed by sputtering of different amounts of In to obtain the

desired composition. The as-deposited nanoparticle ensembles were exposed to ambient conditions after removal from the growth reactor, which led to their oxidation in air and formation of mixed oxide shells encapsulating the bimetallic alloy cores.¹⁸⁻²⁰ The morphology and composition of the nanoparticles were investigated by transmission electron microscopy (TEM) in a JEOL 2100F field-emission microscope equipped with energy dispersive X-ray spectroscopy (EDS), in scanning TEM mode (beam size: 2Å). Laboratory X-ray photoelectron spectra (XPS) on nanoparticle ensembles deposited on Ge(111) were acquired at room temperature using a Specs Phoibos 100 MCD hemispherical analyzer, using excitation by Al K α ($h\nu = 1486.6$ eV) radiation at 300 W (10 keV; 30 mA). XPS spectra were acquired with pass energy of 25 eV and energy step of 0.05 eV. The base pressure in the analysis chamber was in the range of $2-6 \times 10^{-9}$ Torr. The C 1s binding energy (284.8 eV) was used as binding energy reference. To determine the composition in the outermost surface layer, low-energy ion scattering spectroscopy (ISS) measurements were carried out in a UHV system with $1-3 \times 10^{-10}$ Torr base pressure, using 2 keV He ions (Specs IQE 12/38 ion source).

Cyclic voltammetry (CV) of ITO electrodes modified with Au-In alloy-oxide core shell nanoparticles, prepared as described above, was carried out in an Autolab PGSTAT128N potentiostat/galvanostat using a three-electrode cell. Ag/AgCl KCl 3M was used as a reference electrode; the counter electrode was a platinum plate. ITO glasses covered with Au-In nanostructures with different compositions were used as the working electrode. Experiments were carried out in the bias range from -0.8 to 1.0 V using KCl 0.1 mol L⁻¹ as supporting electrolyte in which hydroquinone (HQ) was dissolved to obtain a final concentration of 10^{-3} mol L⁻¹. The scan rate used in CV was 100 mV s⁻¹, with the influence of the scan rate analyzed in the range from 25 to 500 mV s⁻¹.

3. Results and Discussion

Figure 1 summarizes the structure and morphology of nanostructured $\text{Au}_x\text{In}_{1-x}$ alloys with different compositions, produced by sequential vacuum deposition of Au and In, as well as pure Au nanoparticles. The TEM images show that magnetron sputtering yields discrete Au nanoparticles with a large variety of sizes (figure 1 (a)), while the typical morphology that we obtain for a wide composition range of Au-In bimetallic alloys following room temperature oxidation in air (figure 1 (b) – (d)) are elongated, meandering nanostructures and nanoparticles exhibiting a high-surface area morphology. The TEM images also show the partial dewetting of the Au-In alloy into stripes, between which the amorphous C support is exposed. High-resolution TEM (figure 1 (b) – (d), inserts)) shows that the meandering nanostructures consist of a crystalline core with darker contrast and interspersed areas with brighter contrast that stem from the amorphous oxide shells, similar to our earlier observations.¹⁸ Scanning electron microscopy (SEM) investigation on ITO electrodes and crystalline Ge substrates confirms that the Au-In nanostructures have the same morphology, independent of the support. The surface coverage increases with the increase of In content, both because the amount of deposited metal was larger and because the resulting oxides were thicker (see figure 2 (b) and (c), below). Experimental electron diffraction patterns for the four different samples (figure 1 (a') – (d')) are compared to simulated diffraction patterns for Au, orthorhombic Au_3In ,²¹ and cubic AuIn_2 ²² structures and confirm the crystal structure and compositions of the cores. Crystallographic studies of bulk $\text{Au}_{0.5}\text{In}_{0.5}$ found that it adopts a pseudo-orthorhombic structure²³, however the atomic positions have not been reported so far, so we could not simulate the DP for this composition. The $\text{Au}_{0.5}\text{In}_{0.5}$ nanostructures were identified unambiguously from the EDS and XPS measurements (see figures 2 and 3 below). It is worth noting that we find the structures with $\text{Au}_{0.5}\text{In}_{0.5}$ composition showing distinct

diffraction patterns different from the DPs of the other alloys, which confirms that $\text{Au}_{0.5}\text{In}_{0.5}$ represents a distinct crystalline phase and can be used for the identification of this alloy as well.

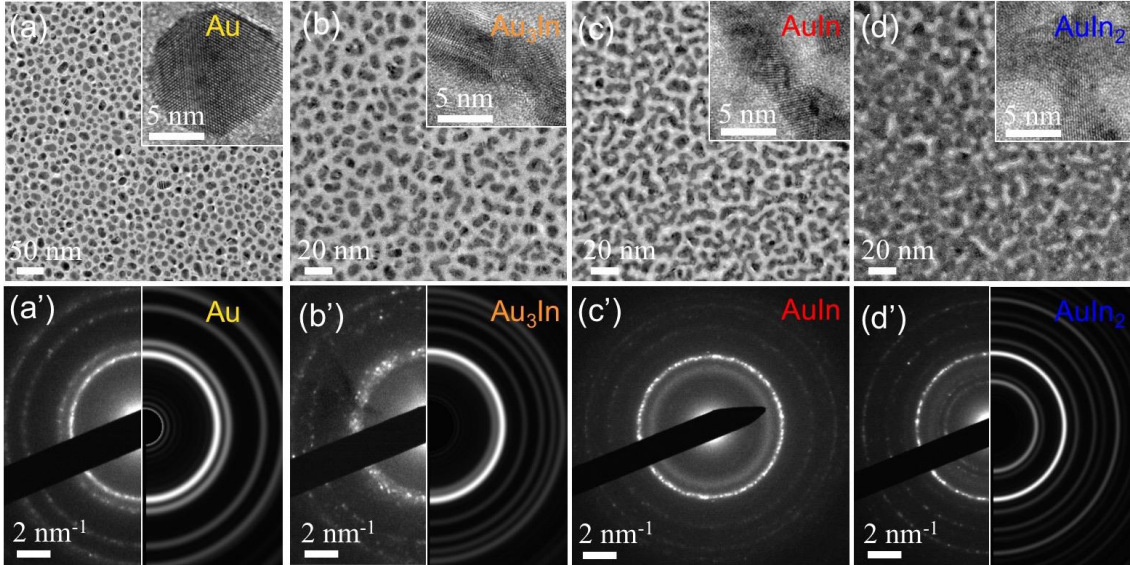


Figure 1: Overview TEM images of the characteristic structure of **(a)** Au and **(b)-(d)** Au-In samples with different compositions (**(b)** Au_3In ; **(c)** AuIn ; **(d)** AuIn_2) prepared by magnetron sputtering. High-resolution TEM images showing details of the crystalline Au nanoparticles and Au-In nanostructures terminated by amorphous surface oxides are shown in the insets of figures (a) – (d). **(a') – (d')** Electron diffraction patterns from the nanostructures in (a) – (d) taken with a 150 nm aperture. The experimental diffraction patterns shown in the left half of each panel are compared to simulated diffraction patterns (right half) calculated using the software package JEMS for nanoparticles with Au, orthorhombic Au_3In ,²¹ and cubic AuIn_2 ²² structures.

EDS measurements were used to confirm the different compositions of the nanostructures depending on the amounts of Au and In deposited. Figure 2 (a) shows characteristic EDS spectra from Au_3In , AuIn , and AuIn_2 nanostructures. The spectra confirm the alloying of the sequentially deposited metals at room temperature.^{18, 24} Following air exposure, amorphous oxide shells that contain both Au and In cover the surface of the Au-In alloy nanostructures (figure 2 (b)). Analysis of the TEM images (figure 2 (c)) shows that the thickness of the oxide shells depends on the composition of the initial Au-In alloy: 1.0 ± 0.4 nm for Au_3In ; 1.8 ± 0.8 nm for AuIn ; and 2.8 ± 1.2 nm

for AuIn₂ nanostructures. This trend in the oxidation rate with alloy composition is the same as the one established for discrete Au-In particles.¹⁸ The amorphous mixed oxide forming on the surface of the particles during room temperature oxidation in air scales with In content, *i.e.*, the oxide shells are thicker for In-rich nanoparticles.

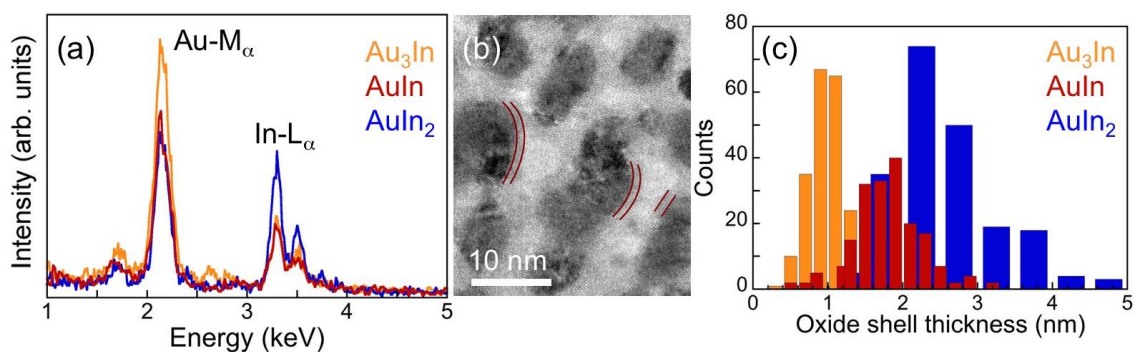


Figure 2: (a) EDS spectra from Au-In nanostructures with different alloys compositions (Au₃In, AuIn, AuIn₂). (b) High-resolution TEM image showing detail of the crystalline AuIn nanostructures terminated by an amorphous surface oxide after exposure to air at room temperature. (c) Thickness distribution of the amorphous oxide shells formed after oxidation in air for 28 days for three different as-deposited alloy compositions.

We further investigated the core-shell Au_xIn_{1-x} oxide nanostructures using XPS to determine the composition and chemical environment, and ISS to identify the elements in the outermost layer of the oxide shell. Both investigations were performed on oxidized nanostructures on Ge support. XPS (in conjunction with TEM) is used to monitor the thickening of the oxide on the surface until the oxide reaches its limiting thickness, identified by the absence of further changes in the XPS spectra. For the Au-In alloys investigated here, this limit was reached after ~21 days in air. XPS on all Au₃In, AuIn, and AuIn₂ nanostructures reveals the presence of Au, In, and O. The Au 4f and In 3d XPS spectra for these three alloy compositions together with reference spectra for a 2 nm Au film and pure In₂O₃ nanoparticles (on Ge) are shown in figure 3 (a) and (b), respectively. As expected the Au 4f spectra of the oxidized alloys are shifted to higher binding energy compared to the Au reference and the observed shifts increase with increasing In content, in good agreement with previous results on Au-In alloys.²⁵ The In

3d peaks for the three alloys are also shifted compared to the spectrum of pure In_2O_3 nanoparticles.

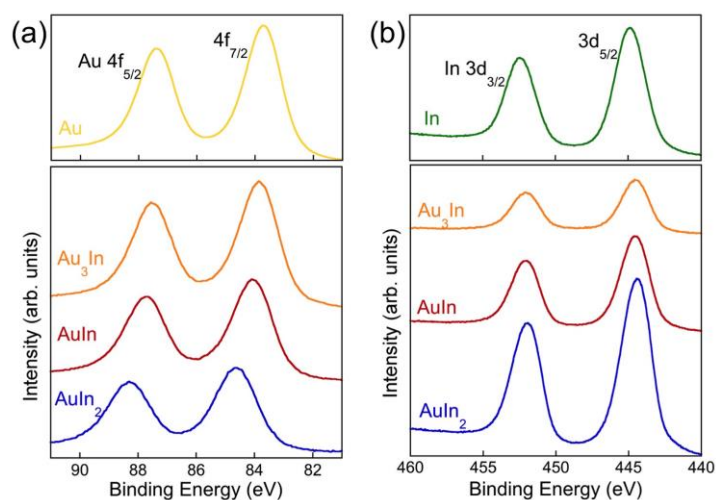


Figure 3. (a) X-ray photoelectron spectra of the Au 4f core levels of the composite Au-In-amorphous oxide core-shell nanostructures compared to a reference spectrum of Au nanoparticles. (b) X-ray photoelectron spectra of the In 3d core levels from the nanostructures compared to a reference sample of In_2O_3 nanoparticles on Ge substrate.

Because of the high energy of the exciting photons from a laboratory XPS source, the kinetic energy of the Au 4f and In 3d photoelectrons is high, which translates into a large escape depth. As a result the XPS measurements probe both the alloy core and the mixed oxide shell of the nanostructures and are of limited use for characterizing the near-surface composition of the Au-In oxide structures, which is key to their electrocatalytic properties. We thus used ISS to determine the constituents of the surface of oxidized Au-In alloy nanoparticles (figure 4 (c) – (e)), with a bulk Ge crystal (with native oxide, figure 4 (a)), a Au film on Ge (figure 4 (b)), and In_2O_3 nanoparticles on Ge (figure 4 (f)) serving as reference samples.

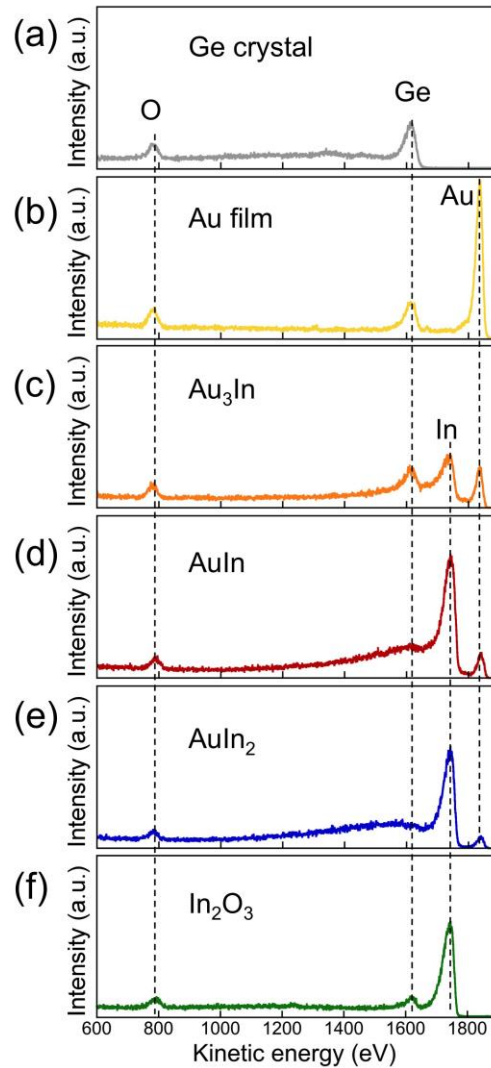


Figure 4. Ion scattering spectra of: **(a)** Reference Ge wafer, used as a substrate for the nanostructures. **(b)** Reference Au film. **(c) – (e)** Au_3In -, AuIn -, and AuIn_2 -amorphous Au-In oxide core-shell nanostructures, respectively. **(f)** Crystalline In_2O_3 nanoparticles.

ISS on the nanostructured Au-In oxide samples shows the presence of Au, In, Ge, and O in the surface layer (figure 4 (c) – (e)). This confirms that all oxidized Au-In nanostructures contain Au at the surface of their oxide shells. The Ge signal stems from the exposed substrate between the nanoparticles. In the alloy nanostructures with higher In content (*i.e.*, larger overall coverage of deposited metal) the Ge peak is not well resolved due to the small remaining area of the bare support in these samples (figure 1 (d)). These samples have the thickest oxide shells (see figure 2 (c)), which contribute to the almost complete shielding of the substrate from the incoming He ions. The (Au:In) peak ratios in samples with different In content show a clear trend in Au content, which

follows the composition of the initial Au-In alloy: the oxide surface of particles with Au₃In cores contains significantly more Au (Au:In = 0.79) than that of particles with AuIn cores (Au:In = 0.22), which again is larger than that of particles with AuIn₂ cores (Au:In = 0.11). From the ISS measurements, we conclude that the outermost atomic layer of the amorphous oxide shells contains Au, In and O. The amount of Au exposed at the oxide surface is not fixed, but can be varied by adjusting the Au concentration in the initial Au-In binary alloy. This provided us access to working electrodes with systematically different concentrations of near-surface Au, stabilized on the amorphous Au-In oxide shells, for electrochemical characterization.

The electrocatalytic properties of the Au-In alloy nanostructures for the detection of hydroquinone were measured in aqueous solutions containing 10⁻³ mol L⁻¹ HQ. This particular concentration was chosen to facilitate comparison with other means of detection, as it is the one usually targeted for HQ detection. Cyclic voltammograms were measured using ITO electrodes modified with the core-shell nanostructures with different (Au:In) ratios. Reference voltammograms were recorded for unmodified ITO and bulk Au electrodes, as well as working electrodes modified with Au nanoparticles. According to the literature, in aqueous solution with neutral pH and using carbon electrodes, *para*-hydroquinones undergo a two-electron single-step oxidation²⁶ that appears as a broad and irreversible anodic peak in the 0.7 – 1.0 V region. The characteristic voltammograms registered using unmodified ITO-on-glass electrodes, bulk gold and Au nanoparticles modified ITO electrodes are compared in figure 5 (a). The voltammograms measured with unmodified ITO and ITO modified with the Au-In nanostructures as the working electrode, are shown in figure 4 (b). In figure 4, all voltammograms are shown on the same scale to allow direct comparison of the currents. In figure 5, the voltammograms registered with the different electrodes are shown on different scales, so that their details can be clearly seen. The characteristic

voltammogram registered using unmodified ITO as the working electrode, is shown in figure 5 (a) (black curve) and figure 6 (a). Starting at 0.75 V, a small increase in the current is observed, indicating that with an unmodified ITO working electrode HQ oxidation starts at high voltages, probably due to the difficulty of the electron transfer to the ITO glass. Thus, unmodified ITO electrodes are not suitable for the detection of hydroquinone.

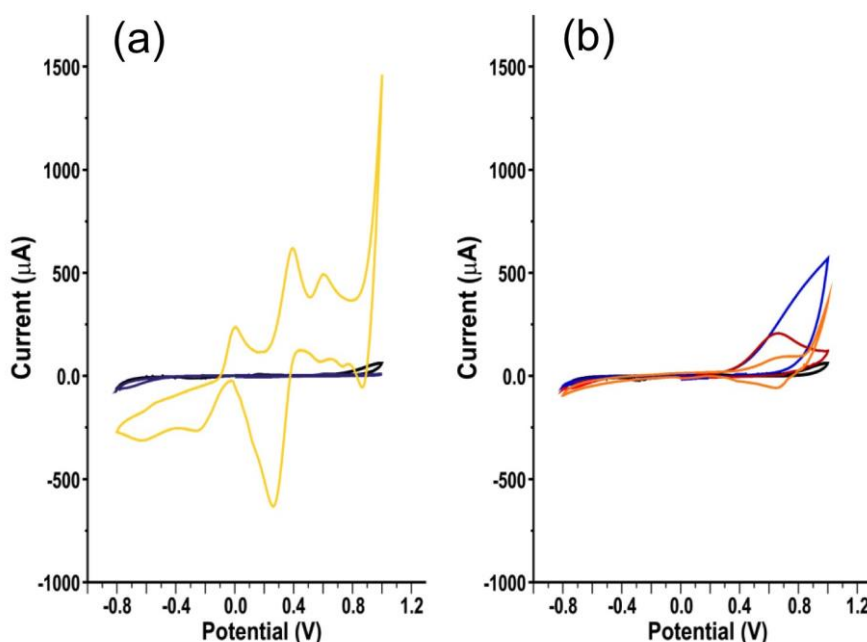
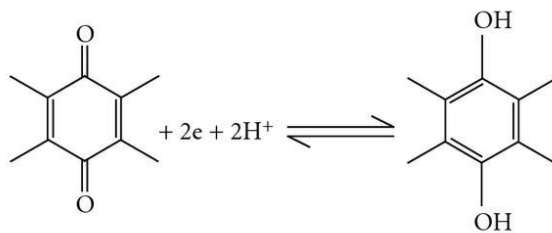


Figure 5. Cyclic voltammograms of **(a)** ITO (black), bulk Au electrodes (dark blue) and Au nanoparticle modified ITO electrodes (yellow curve) and **(b)** ITO electrodes (black), and electrodes modified with AuIn₂ (blue), AuIn (red) and Au₃In (orange) core-amorphous mixed oxide shell nanostructures immersed in an aqueous HQ solution (1 mmol L⁻¹). Scan rate 100 mV s⁻¹.

The voltammogram recorded with a bulk gold working electrode is shown in Figure 5 (a, dark blue curve) and 6 (b). The entire curve presents very low intensity. Despite the low overall intensity, the voltammogram (figure 6 (b)) shows a well-defined redox pair at ~ 0.7 V and ~ 0.2 V (labeled I_a and I_c), respectively. This redox process is associated with the two-electron (reduction-) oxidation process of the quinone-hydroquinone couple in buffered aqueous media²⁶ (Scheme 1) that can be written as:

$$\text{QH}_2 \rightarrow \text{Q} + 2\text{H}^+ + 2\text{e}^-.$$



Scheme 1: Two-electron two-proton reduction of quinone in aqueous buffer.

For the bulk Au electrode, several additional peaks are observed as well. The most important is the redox pair III, which is related to a weak dimerization process of the quinoid form. Notice that peak III_a can be clearly observed, whereas peak III_c overlaps with peak I_c. In addition, several cathodic peaks arising from redox processes associated with adsorbates on the gold surface (usually –OH of the solvent linked to the gold surface) are detected.²⁷ Importantly the current densities recorded with the bulk Au electrode are very low, rendering it almost inert and not suitable to efficiently detect the oxidation of HQ.

The coverage of the ITO/glass electrodes with nanoparticles induced new reaction mechanisms leading to significant changes in the cyclic voltammograms. The voltammograms registered using ITO/glass electrodes with Au nanoparticles with broad distribution of sizes in the range between 1 nm and 20 nm, (Figure 5 (a, yellow curve) and 6 (c)), was characterized by a drastic increase in intensity. In addition, the presence of gold nanoparticles changes the mechanism of oxidation and the HQ molecules undergo a two-step one-electron oxidation. This leads to a new peak (II_a) which is clearly observed at ~0.0 V corresponding to the first one-electron oxidation, while the second one-electron oxidation corresponds to peak Ia.

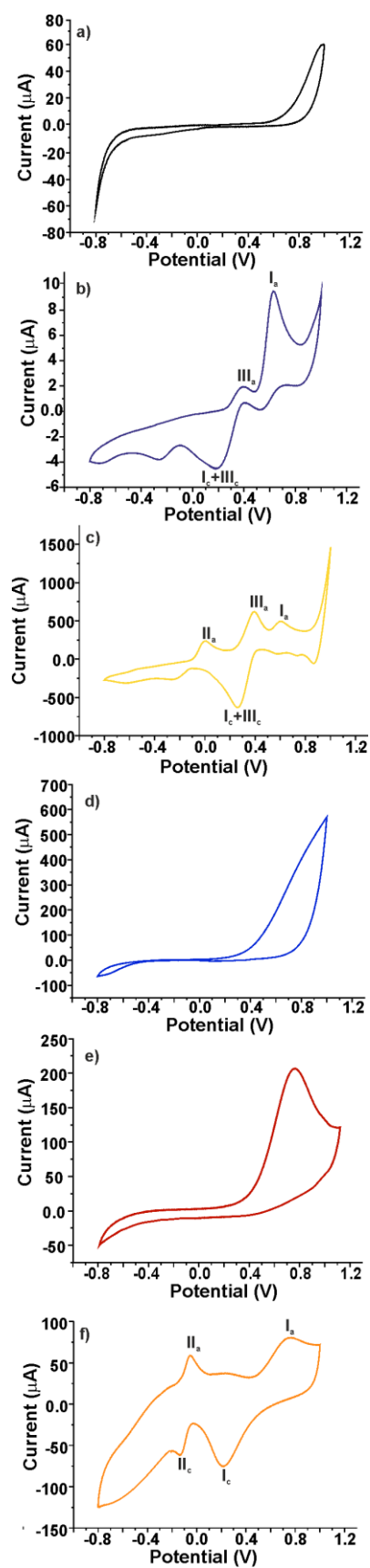


Figure 6. Cyclic voltammograms of (a) ITO, (b) bulk Au electrodes, and electrodes modified with (c) Au nanoparticles, (d) AuIn_2 , (e) AuIn and (f) Au_3In core-amorphous mixed oxide shell nanostructures immersed in HQ (1 mmol L^{-1}). Scan rate 100 mV s^{-1} .

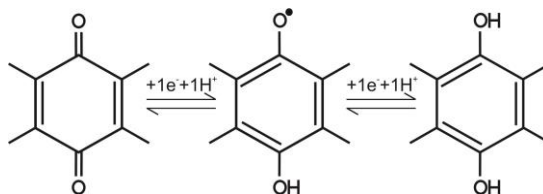
In this case, the number of dimers is higher justifying the change in the relative intensities I_a/III_a . Other cathodic peaks observed are related to the redox process associated with adsorbates on the gold surface, similar to the bulk Au electrode. The current densities are large and thus there is high electrocatalytic activity stemming from the Au nanoparticles. However, the CV is quite complicated due to the activation of several processes such as HQ oxidation, dimerization, etc.

We now discuss results for ITO working electrodes modified with Au-In nanostructures with bimetallic core and oxide shell. A characteristic voltammogram recorded with a working electrode modified by oxidized $AuIn_2$ is shown in figure 5 (b) and figure 6 (d). The voltammogram is rather simple. The onset of the oxidation peak is shifted by ~ 0.3 V to lower potential compared to the ITO electrode, and the increase of the current is much larger.

The changes in the voltammograms are even more pronounced for ITO electrodes modified with AuIn core-oxide shell nanoparticles (Figures 5 (b), 6 (e)). Here the onset of oxidation is again shifted to lower potentials, similar to the $AuIn_2$ modified electrode. In addition, a well-defined peak with an onset at 0.25 V and maximum at ~ 0.55 V is observed. This behavior is consistent with the two-electron oxidation of quinone-hydroquinone couples in buffered aqueous medium.²⁸

On the extreme Au-rich side, finally, ITO electrodes modified with oxidized Au_3In core-shell nanoparticles produced a fundamentally different response. Two separate anodic waves I_a and II_a accompanied by their corresponding reduction peaks I_c and II_c were observed (figures 5 (b), 6 (f)). This behavior is consistent with two successive one-electron oxidation steps (Scheme 2) in which the first step is completely reversible, leading to the formation of semiquinone, and the second quasi-reversible step gives rise to the quinone. Such a behavior has previously been reported in aprotic

solvents,²⁹ but this is the first time that this two-step oxidation process has been found in aqueous media.



Scheme 2: Two-electron two-step one-electron oxidation of quinone in aqueous buffer.

From the above results, it can be concluded that Au-In core-shell nanoparticles show clear electrocatalytic effects that depend on the Au/In ratio of the initial alloy, which in turn determines the amount of Au stabilized in the near surface area of the oxide on the surface of these nanostructures. ITO working electrodes modified with nanoparticles with moderate Au content (AuIn_2 and AuIn) caused a shift of the oxidation peak to lower potentials (*i.e.*, facilitated the oxidation) and showed much higher activity than unmodified ITO electrodes. Importantly for the detection of HQ, the electrocatalytic (reduction-) oxidation of HQ on these electrodes follows a single pathway, the two-electron oxidation of the quinone-hydroquinone couple. This contrasts with the behavior of Au nanoparticle modified ITO electrodes, which also showed large current densities (*i.e.*, high activity) but were not selective to a single reaction mechanism and instead showed a number of concurrent processes. Au-rich Au_3In nanoparticle electrodes not only facilitated the oxidation, but they also provided a different pathway, a two-steps mechanism involving two successive one-electron oxidation steps, to the oxidation of hydroquinone. In general, dimerization and polymerization are avoided when Au-In nanoparticles are used in working electrodes, showing more stable responses and clearer curves. Finally, we note that the Au/In ratio influenced the intensity of the responses. The intensity of the oxidation peaks was higher when the mechanism was a two-electron process, and the intensity was much higher at low Au content.

The influence of the scan rate on the peak height was also investigated in the 25-500 $\text{mV}\cdot\text{s}^{-1}$ range. The redox peak currents increased progressively with the scan rate (figure 7 (a)). The intensity of the peak current (measured at the voltage of oxidation or reduction of hydroquinone) scales with the square root of the scan rate (figure 7 (b)), which indicates a diffusion controlled mechanism for the oxidation/reduction of the antioxidant. This indicates that the high surface area of the nanostructured electrode material facilitates a rapid electron transfer between electrode surface and the analyte.

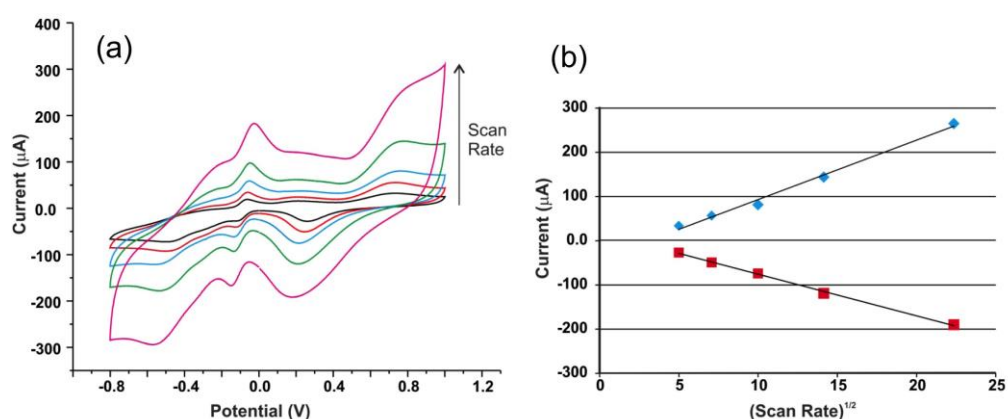


Figure 7. (a) CVs obtained for HQ ($10^{-3} \text{ mol L}^{-1}$) at a Au_3In modified electrode at different scan rates (25-500 $\text{mV}\cdot\text{s}^{-1}$). (b) Plot of peak current, measured at the voltage of oxidation or reduction of hydroquinone, as a function of $(\text{scan rate})^{1/2}$.

The slopes obtained of the peak current vs. $(\text{scan rate})^{1/2}$ characteristics for the oxidation peak are different for the different alloys (Table 1). A higher value of the slope indicates faster charge transfer. The highest value was found for AuIn nanoparticles, indicating that AuIn modified working electrodes were most effective in facilitating the electrode-to-analyte charge transfer.

Sensor	Slope ($\mu\text{A}\cdot(\text{mV}/\text{s})^{-1/2}$)		R^2	
	Oxidation	Reduction	Oxidation	Reduction
AuIn_2	2.4 ± 0.2	-	0.993	-
AuIn	55.0 ± 3.8	-	0.994	-
Au_3In	13.4 ± 0.2	9.4 ± 0.1	0.992	0.998

Table 1. Slope and regression coefficient of linear fits of the intensity of the anodic and cathodic peaks of the hydroquinone redox process as a function of the square root of the scan rate (between 25 - 500 $\text{mV}\cdot\text{s}^{-1}$).

The effect of the concentration of HQ on the response of the sensors was investigated in the range of 10^{-5} to 10^{-3} M. The sensitivity was obtained from the slope

of the graph. The corresponding Limits of Detection (LOD) were calculated according to the $3s_b/m$ criterion, where m was the slope of the calibration graph, and s_b was estimated as the standard deviation ($n = 5$) of the signals at the concentration level corresponding to the lowest concentration of the calibration plot. The obtained results are shown in Table 2.

	AuIn₂	AuIn	Au₃In	Au NPs	Au bulk
Sensitivity	-	0.201	0.075	0.487	0.005
LOD	-	1.33×10^{-5}	3.57×10^{-5}	5.49×10^{-6}	5.05×10^{-4}

Table 2. Sensitivity and LOD towards HQ for ITO working electrodes modified with different oxidized Au-In nanostructures, compared to Au NP and bulk Au electrodes. Relative standard deviation: 1.8% (Au₃In) and 7-8% (AuIn, Au NPs, bulk Au).

The detection limit decreased when increasing the amount of Au exposed on the amorphous oxide surface. The LODs were determined to be in the range of 10^{-5} - 10^{-6} M and were lower than those obtained using bulk Au. However, it is important to note that the nanostructures with AuIn₂ cores did not show good electrocatalytic properties and the peaks associated to HQ shifted to even higher potentials when increasing the concentration of antioxidant. For this reason, the limit of detection could not be calculated accurately for AuIn₂ films.

To establish the reproducibility of the measurements with the different electrodes the determination of 1.0 mM HQ was repeated six times. The first cycle was always different from the rest of the scans and was not included in the results. Such a behavior is typically observed in chemically modified electrodes and is due to the diffusion of ions inside/outside the films. In the case of Au₃In, subsequent cycles achieved a good reproducibility with a relative standard deviation (RSD) of 1.8%. For the remaining nanostructures the intensity of the signals decreased progressively and the RSD calculated was in the range of 7-8%.

4. Conclusions

Oxidized Au-In core-shell nanoparticles with different compositions were investigated as electrocatalysts for the (reduction-) oxidation of hydroquinone. The nanoparticles were characterized by TEM, XPS and ISS measurements and these combined measurements demonstrated that the amorphous mixed oxide shells formed on the Au-In nanoparticles with different alloy compositions have different amount of Au and In on the surface. ITO electrodes modified with oxidized Au-In core-shell nanostructures present different electrocatalytic activity depending on the amount of Au stabilized on their surfaces. Nanoparticles with AuIn₂ and AuIn core surrounded by oxide shells produced a displacement of the onset of the peak to lower potentials, whereas Au₃In samples caused two separate anodic peaks with their corresponding cathodic waves. We can conclude that among the investigated alloy compositions the oxidized AuIn core-shell nanoparticles promise the best performance for the analysis of antioxidants due to the excellent range where the redox peaks are detected, the excellent definition of the redox peaks with high intensity, and enhancement of the charge transfer.

Acknowledgements

Research carried out in part at the Center for Functional Nanomaterials, Brookhaven National Laboratory, which is supported by the U.S. Department of Energy, Office of Basic Energy Sciences, under Contract No. DE-SC0012704. PIF-Uva, EB-14, CICYT (Grant AGL2012-33535) are gratefully acknowledged.

References

1. Vauzour, D.; Rodriguez-Mateos, A.; Corona, G.; Oruna-Concha, M. J.; Spencer, J. P. E. Polyphenols and Human Health: Prevention of Disease and Mechanisms of Action. *Nutrients* **2010**, *2*, 1106-1131.
2. Zhang, F.; Li, M. A.; Li, W. Q.; Feng, C. P.; Jin, Y. X.; Guo, X.; Cui, J. G. Degradation of Phenol by a Combined Independent Photocatalytic and Electrochemical Process. *Chem Eng J* **2011**, *175*, 349-355.
3. Pistonesi, M. F.; Di Nezio, M. S.; Centurion, M.; Palomeque, M. E.; Lista, A. G.; Band, B. S. F. Determination of Phenol, Resorcinol and Hydroquinone in Air Samples by Synchronous Fluorescence using Partial Least-Squares (PLS). *Talanta* **2006**, *69*, 1265-1268.
4. Cui, H.; Zhang, Q. L.; Myint, A.; Ge, X. W.; Liu, L. J. Chemiluminescence of Cerium(IV)-Rhodamine 6G-Phenolic Compound System. *J Photoch Photobio A* **2006**, *181*, 238-245.
5. Liu, C.; Wang, J.; Yang, Y. L. High-Performance Liquid Chromatography Determination of Antioxidants in Cosmetics after Cloud Point Extraction using Dodecylpolyoxyethylene Ether. *Anal Methods-Uk* **2014**, *6*, 6038-6043.
6. Sakthinathan, S.; Palanisamy, S.; Chen, S.-M.; Wu, P.-S.; Yao, L.; Lou, B.-S. Electrochemical Detection of Phenol in Industrial Pollutant Absorbed Molecular Sieves by Electrochemically Activated Screen Printed Carbon Electrode. *Int. J. Electrochem. Sci* **2015**, *10*, 3319-3328.
7. Campbell, F. W.; Compton, R. G. The Use of Nanoparticles in Electroanalysis: an Updated Review. *Anal Bioanal Chem* **2010**, *396*, 241-259.
8. Kuralkar, M.; Ingle, A.; Gaikwad, S.; Gade, A.; Rai, M. Gold Nanoparticles: Novel Catalyst for the Preparation of Direct Methanol Fuel Cell *IET Nanobiotechnology* [Online], **2015**, *9*, p. 66-70. <http://digital-library.theiet.org/content/journals/10.1049/iet-nbt.2014.0004> (Accessed October 6, 2015).
9. Kilic, M. S.; Korkut, S.; Hazer, B.; Erhan, E. Development and Operation of Gold and Cobalt Oxide Nanoparticles Containing Polypropylene Based Enzymatic Fuel Cell for Renewable Fuels. *Biosens Bioelectron* **2014**, *61*, 500-505.
10. Zhao, Z.; Zhang, M.; Li, Y.; Cheng, S.; Chen, X.; Wang, J. Evaluation of Electrochemically Reduced Gold Nanoparticle—Graphene Nanocomposites for the Determination of Dopamine. *Anal Lett* **2015**, *48*, 1437-1453.
11. Medina-Plaza, C.; Furini, L. N.; Constantino, C. J. L.; de Saja, J. A.; Rodriguez-Mendez, M. L. Synergistic Electrocatalytic Effect of Nanostructured Mixed Films Formed by Functionalised Gold Nanoparticles and Bisphthalocyanines. *Anal Chim Acta* **2014**, *851*, 95-102.
12. Lin, X.; Ni, Y.; Li, S.; Kokot, S. A Novel Method for Simultaneous Analysis of Three [Small Beta]2-Agonists in Foods with the Use of a Gold-Nanoparticle Modified Glassy Carbon Electrode and Chemometrics. *Analyst* **2012**, *137*, 2086-2094.
13. Medina-Plaza, C.; García-Cabezón, C.; García-Hernández, C.; Bramorski, C.; Blanco-Val, Y.; Martín-Pedrosa, F.; Kawai, T.; de Saja, J. A.; Rodríguez-Méndez, M. L. Analysis of Organic Acids and Phenols of Interest in the Wine Industry using Langmuir–Blodgett Films Based on Functionalized Nanoparticles. *Anal Chim Acta* **2015**, *853*, 572-578.
14. Chuang, M.-K.; Lin, S.-W.; Chen, F.-C.; Chu, C.-W.; Hsu, C.-S. Gold nanoparticle-decorated graphene oxides for plasmonic-enhanced polymer photovoltaic devices. *Nanoscale* **2014**, *6*, 1573-1579.
15. Vijayakumar, C.; Balan, B.; Saeki, A.; Tsuda, T.; Kuwabata, S.; Seki, S. Gold Nanoparticle Assisted Self-Assembly and Enhancement of Charge Carrier Mobilities of a Conjugated Polymer. *The Journal of Physical Chemistry C* **2012**, *116*, 17343-17350.
16. Corma, A.; Concepción, P.; Boronat, M.; Sabater, M. J.; Navas, J.; Yacaman, M. J.; Larios, E.; Posadas, A.; López-Quintela, M. A.; Buceta, D.; Mendoza, E.; Guilera, G.; Mayoral, A. Exceptional Oxidation Activity with Size-Controlled Supported Gold Clusters of Low Atomicity. *Nat Chem* **2013**, *5*, 775-781.

17. Zhang, J.; Sasaki, K.; Sutter, E.; Adzic, R. R. Stabilization of Platinum Oxygen-Reduction Electrocatalysts Using Gold Clusters. *Science* **2007**, *315*, 220-222.
18. Sutter, E. A.; Tong, X.; Jungjohann, K.; Sutter, P. W. Oxidation of Nanoscale Au-In Alloy Particles as a Possible Route toward Stable Au-Based Catalysts. *P Natl Acad Sci USA* **2013**, *110*, 10519-10524.
19. Sutter, E.; Ivars-Barcelo, F.; Sutter, P. Size-Dependent Room Temperature Oxidation of Tin Particles. *Particle & Particle Systems Characterization* **2014**, *31*, 879-885.
20. Sutter, E.; Sutter, P. Size-Dependent Room Temperature Oxidation of In Nanoparticles. *The Journal of Physical Chemistry C* **2012**, *116*, 20574-20578.
21. Burkhardt, W.; Schubert, K. Uber Messingartige Phasen Mit A3-Verwandter Struktur. *Z Metallkd* **1959**, *50*, 442-452.
22. Goral, J. P.; Eyring, L. The Gold Indium Thin-Film System - a High-Resolution Electron-Microscopy Study. *J Less-Common Met* **1986**, *116*, 63-72.
23. Schubert, K.; Rosler, U.; Kluge, M.; Anderko, K.; Harle, L. Kristallographische Ergebnisse an Phasen Mit Durchdringungsbindung. *Naturwissenschaften* **1953**, *40*, 437-437.
24. Robinson, M. C.; Slavin, A. J. Indium Adsorption on the Au(111) Surface at Room Temperature. *Phys Rev B* **1996**, *54*, 14087-14092.
25. Jayne, D. T.; Fatemi, N. S.; Weizer, V. G. An X-Ray Photoelectron-Spectroscopy Study of Auxiny Alloys. *J Vac Sci Technol A* **1991**, *9*, 1410-1415.
26. Bailey, S. I.; Ritchie, I. M. A Cyclic Voltammetric Study of the Aqueous Electrochemistry of Some Quinones. *Electrochim Acta* **1985**, *30*, 3-12.
27. Deplanche, K.; Merroun, M. L.; Casadesus, M.; Tran, D. T.; Mikheenko, I. P.; Bennett, J. A.; Zhu, J.; Jones, I. P.; Attard, G. A.; Wood, J.; Selenska-Pobell, S.; Macaskie, L. E. Microbial Synthesis of Core/Shell Gold/Palladium Nanoparticles for Applications in Green Chemistry. *Journal of the Royal Society Interface* **2012**, *9*, 1705-1712.
28. Guin, P. S.; Das, S.; Mandal, P. C. Electrochemical Reduction of Quinones in Different Media: A Review. *International Journal of Electrochemistry* **2011**, *2011*, 22.
29. Gupta, N.; Linschitz, H. Hydrogen-Bonding and Protonation Effects in Electrochemistry of Quinones in Aprotic Solvents. *J Am Chem Soc* **1997**, *119*, 6384-6391.

TOC Figure:

